

# Open Research Online

---

The Open University's repository of research publications and other research outputs

## A notch filter for ship detection with polarimetric SAR data

### Journal Item

#### How to cite:

Marino, Armando (2013). A notch filter for ship detection with polarimetric SAR data. IEEE Journal of Selected Topics in Applied Earth Observations and Remote Sensing, 6(3) pp. 1219–1232.

For guidance on citations see [FAQs](#).

© 2013 IEEE

Version: Accepted Manuscript

Link(s) to article on publisher's website:

<http://dx.doi.org/doi:10.1109/JSTARS.2013.2247741>

---

Copyright and Moral Rights for the articles on this site are retained by the individual authors and/or other copyright owners. For more information on Open Research Online's data [policy](#) on reuse of materials please consult the policies page.

---

[oro.open.ac.uk](http://oro.open.ac.uk)

# A Notch Filter for Ship Detection with Polarimetric SAR Data

Armando Marino, *Member, IEEE*

## Abstract

Ship detection with Synthetic Aperture Radar (*SAR*) is a major topic for the security and monitoring of maritime areas. One of the advantages of using *SAR* lay in its capability to acquire useful images with any-weather conditions and at night time. Specifically, this paper proposes a new methodology exploiting polarimetric acquisitions (dual- and quad-polarimetric).

The methodology adopted for the detector algorithm was introduced by the author and performs a perturbation analysis in space of polarimetric targets checking for coherence between the target to detect and its perturbed version on the data. In the present work, this methodology is optimized for detection of marine features. In the end, the algorithm can be considered to be a negative (notch) filter focused on sea. Consequently, all the features which have a polarimetric behavior different from the sea are detected (i.e. ships, icebergs, buoys, etc). Moreover, a dual polarimetric version of the detector is designed, to be exploited in the circumstances where quad polarimetric data cannot be acquired.

The detector was tested with TerraSAR-X quad polarimetric data showing significant agreement with the available ground truth. Moreover, the theoretical performances of the detector are tested with Monte Carlo simulations in order to extract the probabilities of detection and false alarm. An important result is that the detector is, up to some extend, independent of the sea conditions.

## Keywords

Synthetic Aperture Radar, Radar Polarimetry, Ship detection, TerraSAR-X.

Armando Marino is with the ETH Zurich, Institute of Environmental Engineering, Zurich, Switzerland (e-mail: marino@ifu.baug.ethz.ch).

## I. INTRODUCTION

The aim of the work described in this paper is the development of an innovative ship detector, based on Synthetic Aperture Radar (SAR) polarimetry and the methodology pioneered in [1], [2], [3], [4], namely *perturbation analysis*. Ship detection is a key topic for the surveillance of maritime areas largely due to the capability to acquire valuable images independent of solar illumination and (to some extent) weather conditions [5]. In the new procedure, targets are detected by exploiting the difference between the polarimetric characteristics of sea clutter and the targets of interest (e.g. ships, icebergs, etc).

In the literature, several works have described ship detection using radar polarimetry [6], [7], [8], [9], [10], [11] and they are based both on physical and statistical methodologies. The algorithm proposed in this paper is based on a physical rather than a statistical technique and it will be referred to as *Geometrical Perturbation-Polarimetric Notch Filter* (GP-PNF). Please note, the name Polarimetric Notch Filter was already introduced in the past by at least two more authors [12], [13], [14]. The algorithm proposed in this paper is based on a completely different methodology based on a Geometrical Perturbation analysis, as described in the following.

As for an ordinary notch filter, the algorithm rejects the selected target (in our case the sea) and detects anything different from it [15], [16], [17]. However, the original Notch Filter operates on the frequency domain (i.e. the Fourier transform of the signal in time), while the proposed Notch Filter is applied on a target polarization space (6 dimensional complex) where the partial targets lay.

In the following a very brief introduction to polarimetry is presented, focusing mainly on the mathematical tools exploited in the development of the detector. A single target is any

24 target scattering an Electromagnetic (*EM*) wave having a fixed polarization in time/space  
 25 [18], [19]. The latter can be characterized using a unique scattering (Sinclair) matrix:

$$[S] = \begin{bmatrix} HH & HV \\ VH & VV \end{bmatrix}, \quad (1)$$

26 or equivalently a scattering vector:

$$\underline{k} = \frac{1}{2} \text{Trace}([S]\Psi_2) = [k_1, k_2, k_3, k_4]^T, \quad (2)$$

27 where  $\text{Trace}(\cdot)$  is the sum of the diagonal elements of the matrix inside and  $\Psi_2$  is a complete  
 28 set of 2x2 basis matrices under a Hermitian inner product [19]. Finally, it is possible to define  
 29 the scattering mechanism (*SM*) as a normalized vector  $\underline{\omega} = \underline{k}/|\underline{k}|$ .

30 Generally, the targets observed by a *SAR* system are not ideal *SM*, but a combination of  
 31 different objects which we refer to as *partial* targets [20], [21]. In order to characterize a  
 32 partial target a single scattering matrix  $[S]$  is not sufficient, since it is a stochastic process  
 33 and second order statistics are required. In this context, the target covariance matrix can be  
 34 estimated:

$$[C] = \langle \underline{k} \underline{k}^{*T} \rangle, \quad (3)$$

35 where  $\langle \cdot \rangle$  is the finite averaging operator. In the cases that medium where the electromagnetic  
 36 wave propagates (i.e. air) is reciprocal and the sensor is monostatic (i.e. same transmitting  
 37 and receiving antenna), the scattering vector in a generic basis is three dimensional complex  
 38 and the covariance matrix is 3x3. In the literature, when  $\underline{k}$  is expressed in the Pauli basis (i.e.  
 39  $\underline{k} = \frac{1}{\sqrt{2}}[HH + VV, HH - VV, 2HV]^T$ ), the covariance matrix takes the name of *coherency*  
 40 *matrix*  $[T]$  [18], [19].

41 The methodology proposed in this paper takes advantage of the polarimetric coherence  
 42 (i.e. normalized cross correlation). If two different *SM*,  $\underline{\omega}_1$  and  $\underline{\omega}_2$ , are considered, the



43 polarimetric coherence is [19]:

$$\gamma_p = \frac{\underline{\omega}_1^{*T} [C] \underline{\omega}_2}{\sqrt{(\underline{\omega}_1^{*T} [C] \underline{\omega}_1) (\underline{\omega}_2^{*T} [C] \underline{\omega}_2)}}. \quad (4)$$

## 44 II. SHIP DETECTION WITH SAR

45 One of the main features of ships in SAR images is a relatively large backscattering signal  
 46 compared with the sea background. The actual intensity of a vessel is dependent on many  
 47 factors as the size, material and generally the presence of metallic reflectors (triangular and  
 48 dihedral) [22]. This led to the idea of using the intensity contrast between ships and sea  
 49 clutter as a feature to discriminate between them. Several methodologies were proposed [23],  
 50 [9], [24], [25], [26], [27], [28], [29], [30], [31]. Most of these techniques set a statistical test  
 51 between target and clutter background. When a likelihood ratio test is exploited the threshold  
 52 is generally set following a Neyman-Pearson methodology [32], fixing the probability of  
 53 detection or false alarm given the probability density functions (pdf) of clutter and target  
 54 [23], [9], [32]. In case the distribution of the target is unknown the test can be set exploiting  
 55 a parameterized pdf for the sea clutter and setting a constant false alarm [24], [28]. The  
 56 latter is often referred as Constant False Alarm Rate (CFAR). Moreover, many algorithms  
 57 try to estimate the sea pdf parameters locally, in order to take into account the sea variability.  
 58 However, this generally leads to a large computational time [9].

### 59 A. Ship detection with Polarimetric SAR

60 Many authors have pointed out that SAR polarimetry may have a valuable contribution in  
 61 improving ship detection [6], [33], [11], [8], [7], [30]. As a simple example, it can be ob-  
 62 served that the simple use of the cross-polarised channel (HV) instead than the co-polarised  
 63 ones (HH or VV) increases substantially the detection performance (for incidence angles

64 smaller than around 50 degrees) [7]. This is because the sea is supposed to not have scat-  
 65 tering contribution in the cross-polarised channel, therefore improving the Signal to Clutter  
 66 Ratio (SCR). Some of the methodologies are statistical [9]. In these techniques, several po-  
 67 larimetric channels are considered as independent measurements of the same target [6], [8],  
 68 [30]. From the analysis provided by [6] and shared by other authors [16], [34], it was shown  
 69 that quad polarimetric modes provide the best detection performance, followed by the dual  
 70 co-polarization combination HH and VV.

71 A second type of polarimetric ship detectors is based on physical scattering properties of  
 72 targets and ships. Shirvany et al and Touzi et al [34], [7] exploited the difference in coherence  
 73 (or degree of polarization) shown by ships and sea clutter, while Nunziata et al [33] uses the  
 74 reflection symmetry properties showed by the sea but not vessels to perform discrimination.  
 75 A different methodology exploits the differences in the polarimetric signature between the  
 76 sea and targets [17], [35], [15], [16] of which more details will be provided in the following  
 77 sections.

### 78 III. PERTURBATION ANALYSIS FOR POLARIMETRIC DATA

#### 79 A. *Partial target detector (PTD)*

The detector developed in this paper takes advantage of the methodology pioneered in  
 [36], [4], that allowed the detection of partial targets (PTD). A complete treatment of the  
 PTD can be found in [3], [36]. The first step is to introduce a vector formalism where each  
 partial target can be uniquely defined with *one* vector. A *feature partial scattering vector* is

introduced:

$$\begin{aligned} \underline{t} = \text{Trace}([C]\Psi_3) &= [t_1, t_2, t_3, t_4, t_5, t_6]^T = \\ &= [\langle |k_1|^2 \rangle, \langle |k_2|^2 \rangle, \langle |k_3|^2 \rangle, \langle k_1^{*T} k_2 \rangle, \langle k_1^{*T} k_3 \rangle, \langle k_2^{*T} k_3 \rangle]^T, \end{aligned} \quad (5)$$

where  $\Psi_3$  is a complete set of 3x3 basis matrices under a Hermitian inner product.  $\underline{t}$  lies in a subset of  $\mathbb{C}^6$  and it has the first three elements real positive and the second three complex, since it is extracted from a Hermitian matrix. The partial target to be detected can be represented with  $\underline{t}_T$  and the perturbed one with  $\underline{t}_P$ . The perturbed version is obtained starting from  $\underline{t}_T$ , with a rotation in the subset of the physically feasible targets. A change of basis is performed which makes the target of interest lies only on 1 component:  $\underline{t}_T = \sigma_T [1, 0, 0, 0, 0, 0]^T$ . In the following, the normalized versions of  $\underline{t}_T$  and  $\underline{t}_p$  will be exploited:  $\hat{\underline{t}}_T = \frac{\underline{t}_T}{\|\underline{t}_T\|} = [1, 0, 0, 0, 0, 0]^T$  and  $\hat{\underline{t}}_p = \frac{\underline{t}_p}{\|\underline{t}_p\|} = [a, b, c, d, e, f]^T$ .

For the sake of brevity, here, only the final expression of the PTD is presented. However, the reader is redirected to [36], [4] where the mathematical derivation is performed employing perturbation analysis:

$$\gamma_d = \frac{1}{\sqrt{1 + \text{RedR} \left( \frac{\underline{t}^{*T} \underline{t}}{|\underline{t}^{*T} \hat{\underline{t}}_T|^2} - 1 \right)}}, \quad (6)$$

where  $\text{RedR}$  stands for Reduction Ratio and more details regarding this parameter will be provide in the following (e.g. section III.C). The detector is finalized setting a threshold on  $\gamma_d$  as:

$$H_0 : |\gamma_d(P_T, P_c)| \geq T \text{ and } H_1 : |\gamma_d(P_T, P_c)| < T, \quad (7)$$

where  $H_0$  is the hypothesis for detection and  $H_1$  for rejection. Details regarding the selection

of the parameters  $RedR$  and  $T$  can be found in [3], [2], [36].

#### B. Geometrical Perturbation-Polarimetric Notch Filter (GP-PNF)

The application proposed in this work is the detection of targets in a background composed exclusively by locally homogeneous clutter, as the sea [15], [16]. To achieve this goal, the general methodology is modified in the form of a notch filter.

Locally, the sea clutter is polarimetrically well characterized. For instance, a widely employed model is the Bragg scattering. However, the strategy followed in this paper consists in avoiding models or assumptions to characterize the sea scattering, with the aim of achieving a larger applicability of the algorithm. The idea behind the GP-PNF is to reject the sea return and extract the remaining features (in a similar way to a target decomposition [20] even though the output is different from ordinary decompositions).

In this way the detector will be focused not just on ships but also on icebergs (depending on the geographic location), buoys, fish farms or any other structure located over the sea. Following the new mathematical formulation, the *partial scattering vector*  $\underline{t}$  of the sea clutter can be completely described by a vector in a six dimensional complex space  $\hat{\underline{t}}_{sea} \in \mathbb{C}^6$ . The most efficient way to obtain  $\hat{\underline{t}}_{sea}$  is by extracting it from the data, since physical models are generally approximations and sometimes they need a priori information to be accurate (e.g. wind speed and direction).

At contrary than the PTD a target of interest cannot be represented by solely one vector  $\underline{t}_T$ , since ships comes with many different shapes and dimensions. Moreover, it was demonstrated that the orientation of ships plays a vital role in the estimation of its polarimetric signature. For this reason, a linear combination of vectors is exploited to represent the targets of interest. In particular, the subset of interest is the one orthogonal to the vec-

118 tor representing the sea and therefore 5 dimensional complex. Such a subset is represented  
 119 with  $\Omega_T$ , hence each target of interest will have a vector  $\underline{t}_T \in \Omega_T$ , with  $\Omega_T \perp \Omega_{sea}$ . In order  
 120 to perform the perturbation analysis as for the PTD, a projection matrix (of rank 5) for the  
 121 subset of interest has to be defined [37]. The projection matrix can be named  $[Pr_T]$ . In the  
 122 basis where the normalized sea clutter represent one axis (i.e.  $\underline{t}_{sea} = [1, 0, 0, 0, 0, 0]^T$ ), the  
 123 projection matrix could simply be

$$[Pr_T] = \frac{1}{\sqrt{5}} \text{diag}(0, 1, 1, 1, 1, 1), \quad (8)$$

124 which is clearly a rank 5 matrix. Subsequently, the diagonal elements of  $[Pr_T]$  are perturbed  
 125 in order to obtain a subset slightly different from the previous one:

$$[Pr_P] = \text{diag}(a, b, c, d, e, f), \quad (9)$$

126 where  $|a|^2 + |b|^2 + |c|^2 + |d|^2 + |e|^2 + |f|^2 = 1$ . In actual fact, the addition of the  $a$  component  
 127 (i.e. first component) allows for a no-null projection of the vectors on the sea subspace  $\Omega_{sea}$ .  
 128 In this paper, a priori information regarding the target to be detected (i.e. the specific vessel)  
 129 are not exploited, for this reason each of the components of the vessel covariance matrix  
 130 are considered equally important. This leads to the expressions  $b = c = d = e = f$  and  
 131  $|a| \ll |b|$ . Any vector  $\underline{b}_T \in \Omega_{sea}$  can be obtained with

$$[Pr_T]\underline{x} = \underline{b}_T, \quad (10)$$

132 where,  $\underline{x} = [x_1, x_2, x_3, x_4, x_5, x_6]^T$  is a generic vector in the  $\mathbb{C}^6$  subset of the physical feasible  
 133 targets [36], [4]. With the same procedure the vector lying in  $\Omega_T$  can be calculated:

$$[Pr_P]\underline{x} = \underline{b}_P. \quad (11)$$

134 As for the PTD, in order to perform the perturbation analysis the weighted inner product  
 135 between the target to detect and its perturbed version has to be performed. The weighting

136 matrix  $[P]$  is built exploiting a Gramm-Schmidt ortho-normalization where the first vec-  
 137 tor is chosen  $\underline{u}_1 = \hat{t}_{sea}$ . The unitary vectors orthogonal to  $\hat{t}_{sea}$  are  $u_i$  with  $i = 2, 3, 4, 5$ .  
 138 Therefore,  $[P] = diag(|\hat{t}_{sea}^* t|^2, |\underline{u}_2^* t|^2, |\underline{u}_3^* t|^2, |\underline{u}_4^* t|^2, |\underline{u}_5^* t|^2, |\underline{u}_6^* t|^2)$  or more compactly  
 139  $[P] = diag(P_1, P_2, P_3, P_4, P_5, P_6)$ . The detector becomes:

$$\gamma_n = \frac{([Pr_T]\underline{x})^{*T} [P][Pr_P]\underline{x}}{\sqrt{\left([Pr_T]\underline{x}\right)^{*T} [P][Pr_T]\underline{x} \left([Pr_P]\underline{x}\right)^{*T} [P][Pr_P]\underline{x}}}. \quad (12)$$

140 After few passages, the following expression can be found:

$$\gamma_n = \frac{1}{\sqrt{1 + \frac{|a|^2}{|b|^2} \frac{|x_1|^2 P_1}{|x_2|^2 P_2 + |x_3|^2 P_3 + |x_4|^2 P_4 + |x_5|^2 P_5 + |x_6|^2 P_6}}}. \quad (13)$$

141  $\underline{x}$  can be any vector in the subset of the physical feasible targets. In particular, if a priori  
 142 information are not available a fair solution is not to favor any component. The author leaves  
 143 as future work the test of different weights for the components based on vessels a priori  
 144 information. To summarize in this work, it is chosen:

$$\underline{x} = \frac{1}{\sqrt{6}}[1, 1, 1, 1, 1, 1]^T, \quad (14)$$

145 which makes the detector equal to

$$\gamma_n = \frac{1}{\sqrt{1 + \frac{|a|^2}{|b|^2} \frac{P_1}{P_2 + P_3 + P_4 + P_5 + P_6}}}. \quad (15)$$

146 In the basis considered, the power of the target of interest is  $P_T = P_2 + P_3 + P_4 + P_5 + P_6$   
 147 and the sea clutter is  $P_{sea} = P_1$ . Substituting these values in (15), the detector becomes:

$$\gamma = \frac{1}{\sqrt{1 + \frac{|a|^2 P_{sea}}{|b|^2 P_T}}} = \frac{1}{\sqrt{1 + RedR \frac{P_{sea}}{P_T}}}. \quad (16)$$

148 In terms of partial vectors the sea clutter power is

$$P_{sea} = |\underline{t}^{*T} \hat{\underline{t}}_{sea}|^2. \quad (17)$$

149 Please note, the squaring is necessary because  $\hat{\underline{t}}_{sea}$  is a unitary vector. The total power is

$$P_{tot} = \underline{t}^{*T} \underline{t}. \quad (18)$$

150 Therefore, the power of the "non-sea" targets is

$$P_T = P_{tot} - P_{sea} = \underline{t}^{*T} \underline{t} - |\underline{t}^{*T} \hat{\underline{t}}_{sea}|^2. \quad (19)$$

151 The detector could be completed by setting a threshold  $T$  to  $\gamma$ :

$$\gamma = \frac{1}{\sqrt{1 + RedR \frac{|\underline{t}^{*T} \hat{\underline{t}}_{sea}|^2}{\underline{t}^{*T} \underline{t} - |\underline{t}^{*T} \hat{\underline{t}}_{sea}|^2}}} > T. \quad (20)$$

152 The previous detector  $\gamma$  is based on the same construction than the PTD, however, some  
 153 further mathematical passage has to be performed in order to make it a notch filter. As  
 154 explained in details in [36], the PTD has a decision rule based on a SCR between target and  
 155 complemental space. However, in ship detection the amount of backscattering coming from  
 156 the sea is function of the ocean's roughness, which is related to many factors as wind speed,  
 157 currents, swells, etc [38], [39]. Therefore, the balance between sea and target defined as SCR  
 158 can vary across the same scene. On the other hand, a notch filter should be independent of the  
 159 magnitude of the component to be cut, but only dependent on the location of this component.  
 160 In order to correct for this effects, the sea backscattering has to be neglected in the analysis.  
 161 This is mathematically accomplished redefining the matrix [P] exploited to set the weights  
 162 of the inner product. In particular,  $\underline{u}_1 = \hat{\underline{t}}_{sea}$  the first element of the matrix [P] has to be set

constant:  $[P] = \text{diag}(c, |\underline{u}_2^{*T} \underline{t}|^2, |\underline{u}_3^{*T} \underline{t}|^2, |\underline{u}_4^{*T} \underline{t}|^2, |\underline{u}_5^{*T} \underline{t}|^2, |\underline{u}_6^{*T} \underline{t}|^2)$ , with  $c \in \mathbb{R}^+$ . Following the same formulation proposed previously, the GP-PNF becomes:

$$\gamma_n = \frac{1}{\sqrt{1 + \text{RedR} \frac{c}{\underline{t}^{*T} \underline{t} - |\underline{t}^{*T} \hat{\underline{t}}_{sea}|^2}}} > T. \quad (21)$$

The constant  $c$  can be incorporated in the parameter  $\text{RedR}$ :

$$\gamma_n = \frac{1}{\sqrt{1 + \frac{\text{RedR}}{\underline{t}^{*T} \underline{t} - |\underline{t}^{*T} \hat{\underline{t}}_{sea}|^2}}} > T, \quad (22)$$

where the symbol  $\text{RedR}$  is formally kept for consistency with previous formulations. Next section is dedicated to the setting of the parameters  $\text{RedR}$  and  $T$ .

In equation 22, the total power minus the power of the sea  $\underline{t}^{*T} \underline{t} - |\underline{t}^{*T} \hat{\underline{t}}_{sea}|^2$  represents the power of the target of interest (e.g. a vessel). When this is high the expression  $\frac{1}{\underline{t}^{*T} \underline{t} - |\underline{t}^{*T} \hat{\underline{t}}_{sea}|^2}$  will be proximal to zero, therefore the denominator of  $\gamma_n$  will be proximal to 1. This returns a  $\gamma_n$  proximal to 1. On the other hand, if there is only sea, the fraction  $\frac{1}{\underline{t}^{*T} \underline{t} - |\underline{t}^{*T} \hat{\underline{t}}_{sea}|^2}$  will be very high (going to infinity) and the denominator of  $\gamma_n$  will go to infinity as well. This will return a value of  $\gamma_n$  proximal to zero. The detector parameters  $\text{RedR}$  and  $T$  define the sensitivity of the detector.

Analyzing the final expression it is also possible to observe the (theoretical) algorithm independence on the sea backscattering.  $\hat{\underline{t}}_{sea}$  appears only in the expression  $\underline{t}^{*T} \underline{t} - |\underline{t}^{*T} \hat{\underline{t}}_{sea}|^2$ , where the sea component is removed from the total return. Please note, the sea backscattering is not included in the constant  $\text{RedR}$ , since the latter is set once for all and has no relationship with the local sea backscattering.

To summarize, in the final expression of the GP-PNF, the detection is set based on the



backscattering of targets after the contribution of the sea is removed. The similarity with a target decomposition is more evident, even though here the decomposed power is inserted in an expression that constrains it between 0 and 1.

### C. Parameter setting

Aim of this section is to make the GP-PNF automatic, which requires an adaptive selection of the detector parameters.

Considering the GP-PNF has two independent parameters, the threshold  $T$  is chosen arbitrarily (e.g.  $T = 0.98$ ) and the *RedR* (Reduction Ratio) is set locally. The *RedR* can be easily set based on the minimum target of interest  $P_T^{min}$  selected for a specific sensor, considering the expected backscattering of vessels. Even though the sea backscattering is removed, a reference state is needed to obtain the rejection of false alarms. The latter are due to a not perfectly homogeneous background or simply the speckle statistics of sea and noise. Therefore:

$$RedR = P_T^{min} \left( \frac{1}{T^2} - 1 \right). \quad (23)$$

A more optimal setting can be accomplished knowing the probability density function (pdf) of the detector  $\gamma_n$ . Unfortunately, the analytical expression is not trivial and the author leaves its derivation as future work. In the next section, more details regarding this are provided performing Monte Carlo simulations. As a final remark, please note, setting a threshold on the minimum target to detect  $P_T^{min}$  the GP-PNF can take into account for some polarimetric heterogeneity. The higher is  $P_T^{min}$  the more heterogeneity is allowed.

Another point to take into account to make the algorithm automatic is that over a large scene the sea polarimetric behavior may change due to local incidence angle, currents, wind effects, etc. This effects are particularly visible in higher frequencies as X-band [40]. How-

203 ever, it can be seen that in a local averaging window the sea continues to behave in a relatively  
 204 homogeneous way. Therefore, the selection of the Notch in the target polarimetric space (i.e.  
 205  $\hat{\underline{t}}_{sea}$ ) has to be performed with local measurements.

206 In this paper a simple procedure is followed for two main reasons: firstly, it will show  
 207 the algorithm capability in a more clear way without alterations consequence of intensive  
 208 pre-processing (where we do not know if the performances are due to the GP-PNF or the  
 209 pre-processing), and secondly, it makes the final algorithm particularly fast. However, in  
 210 the future, more sophisticated methodologies will be investigated with expected increasing  
 211 of performances. In details, a large moving window  $W_{tr}$  is employed to estimate  $\hat{\underline{t}}_{sea}$  and  
 212 inside this area a second smaller moving window  $w$  is exploited to calculate  $\underline{t}$  (the details  
 213 regarding the windows size are presented in the validation section, since they are depending  
 214 to the sensor and target to be detected [9]). The presence of a ship in  $W_{tr}$  is averaged out  
 215 resulting in a value of  $\hat{\underline{t}}_{sea}$  different from the only sea case, but also different from the ship  
 216 alone (or a part of the ship if this is bigger in size than  $w$ ). A solution exploiting guard  
 217 windows was attempted showing not evident improvements. This is mainly due to the fact  
 218 that ships are not homogeneous targets and the target window  $w$  generally includes only a  
 219 portion of the entire ship. For this reason, even in case of hardly corrupted  $\hat{\underline{t}}_{sea}$  a portion of  
 220 ship is expected to be polarimetrically different from the entire ship plus sea. Finally, it is  
 221 important to notice that even if the ship is extraordinarily homogeneous and bright and the  
 222 signature in the training  $W_{tr}$  is exactly equal to the one of  $w$ , the detection will be triggered  
 223 as soon as the target window  $w$  is centered to an area of sea just outside the target (in this case  
 224 the ship will be interpreted as background and the sea as target). This means that the edges  
 225 of the ship (point of discontinuity between sea and ship) will still be detected. A similar  
 226 reasoning could be extended to large icebergs: the algorithms should be able to detect the

edges. Additionally, the local heterogeneity on icebergs may trigger detection on the internal parts as well. However, this are just speculations and the author leaves the test as future work before to provide conclusive statements.

Beside this theoretical reasoning, in the simulation section the issue of estimating  $\hat{t}_{sea}$  is treated and we remind to the following sections for more details regarding this issue.

#### D. Dual polarimetric GP-PNF

In order to characterize uniquely a partial target quad polarimetric data are necessary. However, in some instances the coherent acquisition of four polarizations is not feasible and only two coherent acquisitions can be performed (dual polarimetric mode) [19], [18]. The aim of this section is the development of a version of the algorithm applicable to dual polarimetric data.

The use of dual polarimetric data may also be interesting because for some sensors they are available with higher resolution or swath cover. Clearly, reducing the number of images (observables) the performances of the final algorithm are expected to be lower. Another interesting point leading the author to particularize the detector for this acquisition mode is that the satellite TerraSAR-X is promising to have a significant contribution on ship detection due to its very high resolution achievable from space [40]. However, its quad-polarimetric mode is only experimental.

A dual polarimetric scattering vector can be introduced as  $\underline{k}_d = [k_1, k_2]^T$ , with  $k_1$  and  $k_2$  being complex numbers (for instance  $HH$  and  $VV$ ). The covariance matrix can be estimated as:

$$[C_d] = \begin{bmatrix} \langle |k_1|^2 \rangle & \langle k_1^{*T} k_2 \rangle \\ \langle k_2^{*T} k_1 \rangle & \langle |k_2|^2 \rangle \end{bmatrix}. \quad (24)$$

248 Subsequently, a 3 dimensional partial feature vector can be built:  $\underline{t}_d = Trace([C_d]\Psi_2) =$   
 249  $[\langle |k_1|^2 \rangle, \langle |k_2|^2 \rangle, \langle k_1^{*T} k_2 \rangle]^T$ . Finally, the dual polarimetric GP-PNF is:

$$\gamma_{dn} = \frac{1}{\sqrt{1 + RedR \frac{1}{\underline{t}_d^{*T} \underline{t}_d - |\underline{t}_d^{*T} \hat{\underline{t}}_{dsea}|^2}}} > T, \quad (25)$$

250 where  $\hat{\underline{t}}_{dsea}$  is the normalized dual polarimetric signature of the sea extracted with the large  
 251 window  $W_{tr}$  and  $\underline{t}_d$  is the partial vector extracted with the small window  $w$ .

252 In order to have an intuitive understanding of the differences between quad and dual data  
 253 it has to be kept in mind that with dual-pol only a portion of the polarimetric space is ob-  
 254 servable. In order to obtain a detection, the projection of the target vector  $\underline{t}_T$  in the observed  
 255 dual-polarimetric space must be above the threshold. On the other hand, the null is selected  
 256 considering exclusively the projection of the sea vector  $\underline{t}_{sea}$  over the observed sub-space.  
 257 Therefore, it is clear how a small projection in the dual-pol sub-space may lead to missed  
 258 detection and false alarms respectively. Considering the sea has a behavior generally similar  
 259 to a surface, the use of dual-pol HH/VV should to be theoretically advantageous compared  
 260 to HH/HV.

261 As a summary of the processing performed, Figure 1 presents the flow chart of the algo-  
 262 rithm. Very briefly, the polarimetric data (dual or quad pol) are processed in order to estimate  
 263 the coherency matrices with two different moving windows ( $W_{tr}$  and  $w$ ). Subsequently, the  
 264 matrices are vectorized to obtain the  $\underline{t}$  vectors. The latter accompanied by the detector pa-  
 265 rameters (e.g.  $T = 0.98$  and  $RedR = 2 * 10^{-3}$ ) are used to build the detector. The output of  
 266 the algorithm is a detection mask.

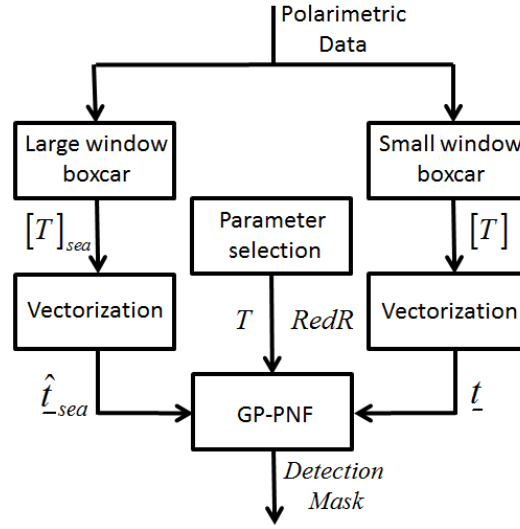


Fig. 1. Flow chart of the detector.

#### IV. SIMULATION

This section has the intention to test the statistical behavior of the GP-PNF. In particular, it will be shown that the GP-PNF is to some extent independent of: (i) the sea backscattering  $\sigma_{sea}$ ; (ii) the specific sea polarimetric signature  $\underline{t}_{sea}$ . While in previous sections the asymptotic solution (eq. 22) shows the mathematical reasons for such independence, here these properties are tested from the statistical point of view. Ideally, the derivation of the probability density function (pdf) of  $\gamma_n$  would provide exact information. However, this is not trivial and the analytical solution may not exist. For this reason, this derivation is left as future work and here a simulation approach is adopted. The properties *i* and *ii* will be verified through a series of simulations based on the TerraSAR-X datasets.

A Monte Carlo simulation was designed, where  $\sigma_{sea}$  and  $\underline{t}_{sea}$  can be arbitrarily modified. In the adopted statistical model, the sea clutter is generated by complex Gaussian random variables, where the asymptotic polarimetric signature is defined by a coherency matrix  $[G_{sea}]$ . The realization of a scattering vector  $\underline{k}_{sea}$  for a generic pixel of sea can be estimated

281 as

$$\underline{k}_{sea} = [G_{sea}]^{-\frac{1}{2}} \underline{u} \quad (26)$$

282 where  $[G_{sea}]$  is the *generating* coherence matrix which represents the asymptotic coherence  
 283 matrix. In this experiment  $[G_{sea}]$  is extracted from the TerraSAR-X data selecting an area  
 284 (200x200 pixels) with visual absence of vessels. The area exploited in this analysis is in-  
 285 dicated by a white rectangle on the Pauli RGB image in Figure 9.b.  $\underline{u} = [u_1, u_2, u_3]^T$  is a  
 286 normalized three dimensional complex vector (i.e.  $\underline{u} \in \mathbb{C}^3$ ) with components complex Gaus-  
 287 sian random variables with zero mean (i.e. the real and imaginary part of each component is a  
 288 zero mean Gaussian random variable with same standard deviation). For the sake of brevity,  
 289 in this paper only quad polarimetric data were simulated, however the dual polarimetric case  
 290 can be easily taken into account.

291 The simulated coherence matrix  $[C_{sea}]$  (and subsequently the vector  $\hat{\underline{t}}_{sea}$ ) is obtained by  
 292 estimating the averaged outer product of independent realizations of  $\underline{k}_{sea}$ . If  ${}^i \underline{k}_{sea}$  is a generic  
 293 realization of  $\underline{k}_{sea}$ , the matrix  $[C_{sea}]$  can be obtained as:

$$[C_{sea}] = \frac{1}{N} \sum_{i=1}^N {}^i \underline{k}_{sea} {}^i \underline{k}_{sea}^{*T} \quad (27)$$

294 The targets of interest are simulated extracting the coherence matrices corresponding to  
 295 real targets in the TerraSAR-X dataset. The coherence matrices for three targets, two ships  
 296  $[C_w]$ ,  $[C_h]$  and a wind turbine  $[C_t]$  were exploited. More details regarding these targets will  
 297 be presented in the following sections. It is inevitable that, to some extent, a component  
 298 from the sea surface will also be contained in  $[C_w]$  and  $[C_h]$ , while  $[C_t]$  does not represent  
 299 the entire turbine, nevertheless these signatures represent some realistic matrices as they can  
 300 be extracted from data. If  $\sigma_{sea} = \|\underline{t}_{sea}\|$  and  $\sigma_T = \|\underline{t}_T\|$  the Signal to Clutter Ratio (*SCR*) as

301 interpreted by the detector can be calculated

$$SCR = \left( \frac{\sigma_T}{\sigma_{sea}} \right)^2. \quad (28)$$

302 Please note, the square is needed because the detector works with power of partial vectors.

303 The target used presents the following values:  $\|t_w\| \approx 7.6$ ,  $\|t_h\| \approx 0.8$  and  $\|t_t\| \approx 19.4$ .

#### 304 A. Independence with respect to $\sigma_{sea}$

305 In this first simulation, the Null for the polarimetric signature of the sea  $\hat{t}_{sea}$  is simply  
 306 extracted from the TerraSAR-X dataset. In this way, the simulation will be closer to a real  
 307 scenario which does not consider any model assumption (except the Gaussian scattering).  
 308 500 simulations were performed with the  $SCR$  varying in the interval  $[-20dB \ 20dB]$ . Each  
 309 simulation considers averaging a defined number of samples ( $N_w$ ). The detection was run  
 310 for each simulation and the probability of detection and false alarm was calculated as

$$P_D = \frac{N_D}{N}, \quad P_F = \frac{N_F}{N}. \quad (29)$$

311 where  $N = 500$  is the total number of simulations (given a fixed  $SCR$ ).  $N_D$  and  $N_F$  are  
 312 respectively the number of detections and false alarms (given a fixed  $SCR$ ). In other words,  
 313 for each one of the 500 values of  $SCR$  the probabilities are calculated over 500 realizations  
 314 each one generated with  $N_w$  samples averaged each other. The value used for RedR is the  
 315 same used for real data:  $RedR = 2 * 10^{-3}$  that returns a minimum target  $P_T^{min} \approx 0.22$ .  
 316 This value was selected observing that all the targets of interest were showing much higher  
 317 values. On the other hand, the value of  $N_w$  adopted in the simulation is 38, since in the real  
 318 data the windows choice provides about 38 Equivalent Number of Looks (ENL).

319 Figure 2 shows the probability of detection  $P_D$  for the experiments. Only one of the three  
 320 plots is presented since the  $P_D$  is steadily equal to one for all the three targets. Clearly, it

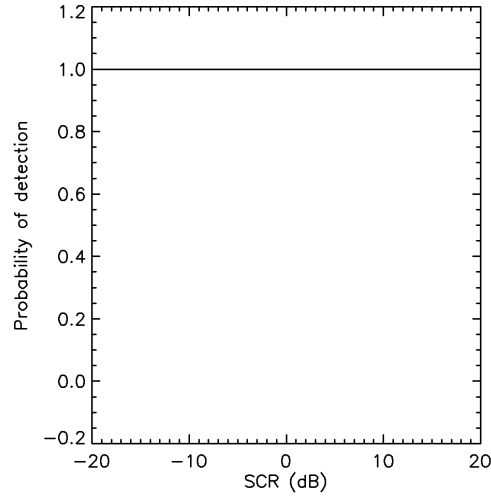


Fig. 2. Simulated probability of detection  $P_D$  for three targets varying the  $SCR$  in the interval  $[-10dB \ 30dB]$

Averaging window: 170 samples. Number of simulations for each  $SCR$ : 500.

has to be considered that the accuracy is related to the quantization error of  $1/2N = 10^{-3}$ . The excellent results are consequence of the capability of the GP-PNF to delete the sea components before to set the threshold. If the final equation of the detector is analyzed (i.e. eq.22), the backscattering from  $\underline{t}_{sea}$  does not appear. Even if the filter is not optimally set, and there is some spillage of sea power on the target subset, this will increase the value of  $\underline{t}^{*T}\underline{t} - |\underline{t}^{*T}\hat{\underline{t}}_{sea}|^2$ , since  $|\underline{t}^{*T}\hat{\underline{t}}_{sea}|^2$  decreases, which increases the value of the detector  $\gamma_n$  (i.e. it provides a stronger detection).

$P_F$  is presented in Figure 3. The horizontal axis represents the intensity of the sea clutter  $\sigma_{sea}$ . The trend of  $P_F$  has a very fast transition point  $\sigma_{sea}^c$  where the value pass from 0 to 1. This is because, in general, small errors in the statistical estimation of  $[C_{sea}]$  are interpreted as a different target. When the intensity from the sea increases, a small estimation error can lead to a relatively high spilling of power in  $\underline{t}^{*T}\underline{t} - |\underline{t}^{*T}\hat{\underline{t}}_{sea}|^2$ , that may exceed  $P_T^{min}$ , triggering a detection. In conclusion, the increase of  $P_F$  is the result of errors in the estimation of the Null. In order to test this last idea, the same analysis was repeated utilizing a smaller and



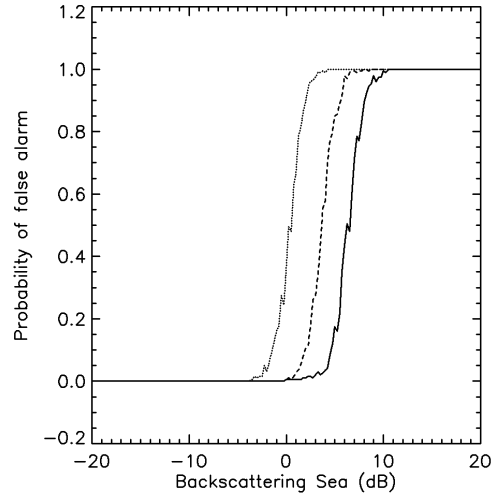


Fig. 3. Simulated probability of false alarm  $P_F$  for three target averaging windows varying the  $SCR$  in the interval  $[-20dB \ 20dB]$ .  $RedR = 2 * 10^{-3}$ . Solid line: 150 independent samples; Dashed line: 38 independent samples; Dotted line: 8 independent samples. Number of simulations for each  $SCR$ : 500.

335 bigger averaging window (respectively 8 and 150 independent samples). This test is also  
 336 interesting in evaluating the sensitivity of the detector respect to the window size exploited.  
 337 Reducing the averaging window, the transition point  $\sigma_{sea}^c$  moves towards the left (i.e. lower  
 338 sea states). Interestingly, the sea is expected to have backscattering in VV always below  $0dB$   
 339 [6] for common incidence angles (above 20 degrees). In other words, with 38 ENL the false  
 340 alarm would be a problem only for unrealistically high values of  $\sigma_{sea}$ .

341 Observing Figure 3 it appears that for a window considering only 8 independent samples  
 342 the false alarms are suppose to start appearing for value of  $\|t_{sea}\| \approx -2dB$  which are values  
 343 that may be found in rough sea conditions. In case that an user would be interested in  
 344 employing a very small target window the minimum target to detect should be increased  
 345 in order to avoid false alarms (i.e. increasing  $RedR$ ). Figure 4 shows the same simulation  
 346 where now  $RedR = 6 * 10^{-3}$ , which corresponds to  $P_T^{min} \approx 0.38$ . With this value of  $RedR$   
 347 it is possible to recover the increase of false alarms showed by the smaller window of 8

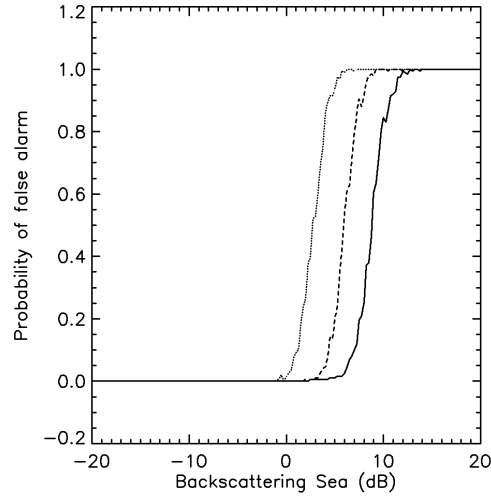


Fig. 4. Simulated probability of false alarm  $P_F$  for three target averaging windows varying the  $SCR$  in the interval  $[-20dB \ 20dB]$ .  $RedR = 6 * 10^{-3}$  Solid line: 150 independent samples; Dashed line: 38 independent samples; Dotted line: 8 independent samples. Number of simulations for each  $SCR$ : 500.

independent samples. The latter test provides also information regarding the sensitivity of the detector with respect to the  $RedR$  parameter.

To conclude, the simulation showed that when the sea is very bright it will introduce false alarms, depending on the averaging window used. Fortunately, the values of sea backscattering required to trigger a false alarm are not expected in real data for incidence angles higher than 20 degrees.

#### B. Dependence on the target backscattering $\sigma_T$

The  $P_D$  estimated in the previous section is particularly good, showing perfect detection. However, in order to do not create false expectations, this section wants to locate the previous results in a larger context showing in which case the  $P_D$  can be smaller than 1.

In the selection of the detector parameters, the  $RedR$  is set with respect to a minimum target to detect (after the filtering). This means that the optimum performance,  $P_D \approx 1$  can be obtained exclusively for  $P_T \geq P_T^{min}$ . Again, the presence of this lower boundary is not a

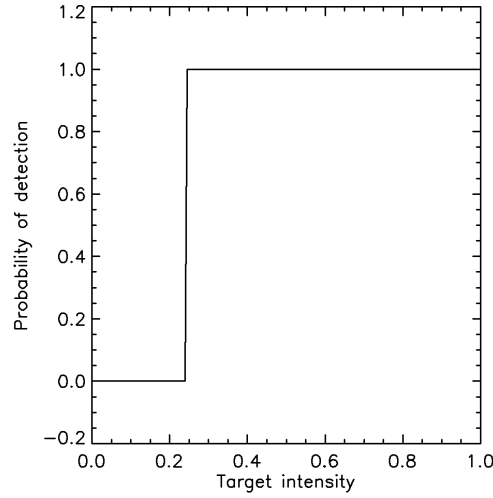


Fig. 5. Simulated probability of detection  $P_D$  for a vessel with intensity  $\|\underline{t}_w\|$  varying in the interval  $[0 \ 1]$  (linear values).  $RedR = 2 * 10^{-3}$  Averaging window: 38 samples. Number of simulations for each intensity: 500.

361 limitation, since it is needed to reject unwanted targets and estimation errors (i.e. due to the  
 362 finite averaging). In order to test this property, Figure 5 shows the detection of the ship  $\underline{t}_w$   
 363 varying its backscattering value (i.e.  $\|\underline{t}_w\|$ ) between 0 and 1.

364  $P_D$  goes from 0 when  $\|\underline{t}_w\|$  is below  $P_T^{min}$  to 1 when it is above  $P_T^{min}$ . The crossing point  
 365 is after 0.22, as set previously with the choice of the RedR. In details, the location of the  
 366 crossing point is around 0.25 because the target  $\underline{t}_w$  is not perfectly orthogonal to  $\underline{t}_{sea}$  and  
 367 the RedR is set considering the complementary space of  $\underline{t}_{sea}$ . However, the closeness of the  
 368 crossing point to 0.22 is a good indicator that the signature of this vessel is quite orthogonal  
 369 to the sea. Similar results were obtained repeating the same analysis with the other two  
 370 targets (even closer to 0.22 for the turbine).

371 The same simulation is repeated in Figure 6 considering  $RedR = 6 * 10^{-3}$  to cover the  
 372 case of very small windows. Here, the crossing point is around 0.42, which is close to the  
 373 theoretical value of 0.38.

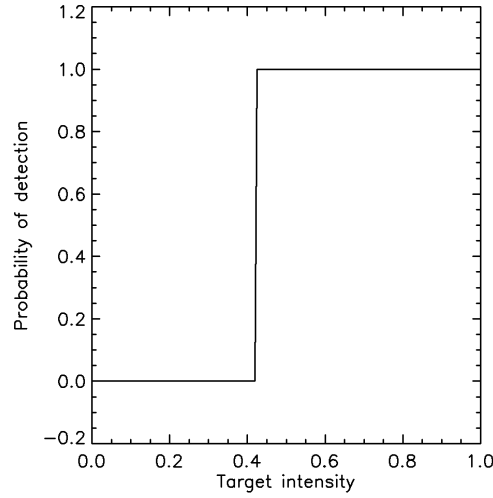


Fig. 6. Simulated probability of detection  $P_D$  for a vessel with intensity  $\|\underline{t}_w\|$  varying in the interval  $[0 \ 1]$  (linear values).  $RedR = 6 * 10^{-3}$ . Averaging window: 38 samples. Number of simulations for each intensity: 500.

374 To conclude, if the target is very weak in the subset orthogonal to the vector representing  
 375 the sea clutter, it will not be detected. This is useful to reject false alarms, but put a lower  
 376 limit to the brightness of a detectable target.

### 377 C. Independence with respect to $\underline{t}_{sea}$

378 The independence of the specific sea polarimetric signature (i.e.  $[C_{sea}]$ ) is investigated.  
 379 In particular, the detector is supposed to have positive performance even if the polarimetric  
 380 entropy [19], [20] of the sea  $H_{sea}$  (calculated as the entropy of the eigenvalues of  $[C_{sea}]$ ) is  
 381 equal to 1 (i.e. completely depolarized targets). This interesting result is consequence of the  
 382 exploitation of the  $\mathbb{C}^6$  space, where each partial target (including the one with entropy equal  
 383 to 1) can be uniquely characterized.

A simulation was performed employing a completely depolarized sea clutter (i.e.  $H_{sea} =$

1):

$$[C_{sea}] = [I], \quad (30)$$

$$\underline{k}_{sea} = \lambda [I]^{-\frac{1}{2}} \underline{u} = \lambda \underline{u}$$

where again,  $\underline{u}$  is a 3 dimensional unitary complex Gaussian vector,  $[I]$  is the identity matrix and  $\lambda$  is a real positive number.  $P_D$  and  $P_F$  are estimated with the same procedure illustrated previously.

The  $P_D$  plots are not presented, for the sake of brevity, since they are always equal to 1. This is because ships are not expected to have a polarimetric behavior equal to thermal noise. Theoretically, the only way to influence the detection through the selection of the Null is when the signature of the sea  $\underline{t}_{sea}$  becomes equal to a class of targets (i.e.  $\underline{t}_{sea} = \underline{t}_{T1}$ ). In this case, this and only this class of targets will be rejected from the detection mask, since it would be interpreted as sea. However, it would be unlikely that the sea surface acquires the same polarimetric scattering behavior of a complex structure as a vessel.

Figure 7 presents the probabilities of false alarm  $P_F$  for a sea clutter simulated as thermal noise. All the other parameters are the same employed in the previous simulation.

The probability of false alarm seems to have changed slightly compared to the previous simulation. In particular, the critical sea backscattering  $\sigma_{sea}^c$  seems to have moved leftward. This effect is again due to the quality of the estimation of the coherence matrix  $[C_{sea}]$ . In particular, the completely depolarized case represents one of the worst scenarios for extracting the second order statistics, since all the off-diagonal terms are theoretically equal to 0. A very large number of samples is necessary to estimate correctly these terms and estimation errors are more visible. Fortunately, the value of  $\sigma_{sea}^c$  for  $ENL = 38$  is still higher than the expected upper boundary of sea backscattering (i.e. less than 0dB), therefore  $P_F$  is supposed

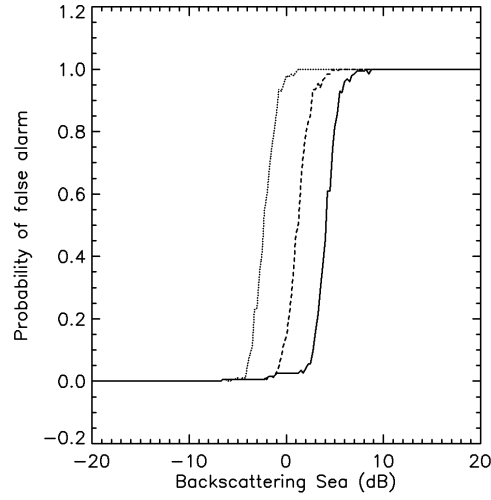


Fig. 7. Simulation of  $P_F$  for sea clutter completely depolarized (thermal noise), varying the intensity of the sea  $\|t_{sea}\|$  between  $[-20dB \ 20dB]$ . Solid line: 150 samples; Dashed line: 38 samples; Dotted line: 8 samples. Number of simulations for each intensity: 500.

404 to remain equal to zero in real data.

405 Summarizing, the algorithm is able to cope with different polarimetric signatures of the  
 406 sea clutter, even though this may impact slightly on the false alarm rate. However, in the  
 407 simulation performed the values at which the false alarms should appear are still unrealistic  
 408 in real data especially because depolarized sea is mainly expected when the signal is very  
 409 low (due to noise effects).

#### 410 *D. Errors in the selection of the Null*

411 In this section, the issue of an highly heterogeneous sea is treated. As explained in the  
 412 theoretical sections,  $t_{sea}$  can change in the same scene therefore the Null has to be set locally.  
 413 However, algorithms for the extraction of  $t_{sea}$  may suffer of errors due to local heterogeneity  
 414 or presence of a target in the averaging cell. Therefore, it is necessary to have some insight  
 415 regarding the detector robustness with respect to these eventual errors.

416 In this simulation,  $t_{sea}$  was calculated as the superposition (in  $\mathbb{C}^6$ ) of two contributions,

one representing the target adopted as the Null (what we think is the sea)  $\underline{t}_{null}$  and one orthogonal to this  $\underline{t}_{\perp}$  (the error that we make):

$$[C_{sea}] = \sigma_{null}[C_{null}] + \sigma_{\perp}[C_{\perp}], \quad (31)$$

where

$$[C_{null}] \leftrightarrow \underline{t}_{null}, [C_{\perp}] \leftrightarrow \underline{t}_{\perp} \quad (32)$$

$$\underline{t}_{null} \perp \underline{t}_{\perp}$$

The amount of error on the estimation of  $\underline{t}_{sea}$  is varied using a parameter defined as:

$$\rho_{sea} = \frac{\|\underline{t}_{null}\|}{\|\underline{t}_{\perp}\|}. \quad (33)$$

The signature of the sea  $\underline{t}_{sea}$  is again extracted from the data in order to provide a more realistic scenario and  $\rho_{sea} = 10$ . The results of this simulation for  $P_D$  are not presented since they are again steadily equal to 1 (i.e.  $P_D \approx 1$ ). The explanation is the same than the previous case.

A different course is suffered by  $P_F$  (depicted in Figure 8). The general trend (i.e. presence of a transition point  $\sigma_{sea}^c$ ) resembles the previous scenario (Figure 3), however, now  $\sigma_{sea}^c$  has moved leftward (lower clutter power). This is because, the error component  $\underline{t}_{\perp}$  lies in the subset of valuable targets and when the sea intensity is high, the projection over the error component can be large enough to trigger a detection. Fortunately, the value of  $\sigma_{sea}^c$  is still particularly high [6].

To conclude, the GP-PNF detector can have problems with false alarms if the sea background is not properly estimated. In a real scenario this translates in possible presence of false alarms when the background is particularly heterogeneous. This is for instance the case

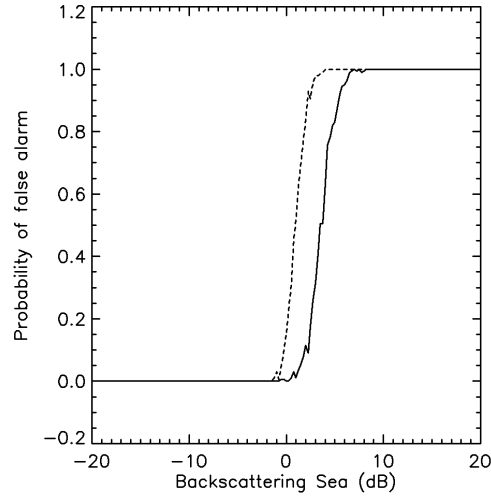


Fig. 8. Probability of false alarm  $P_F$  when the Null is not fixed exactly on the sea signature, varying  $\|t_{sea}\|$  in the interval  $[-20dB \ 20dB]$ . Solid line: no error  $\rho = \infty$ ; Dashed line: 10% error  $\rho = 10$ . Number of simulations for each SCR: 500.

of sea ice clutter, where the GP-PNF in its current formulation would probably not be suited for ship/iceberg detection. Further work has to be carried out in this context.

## V. VALIDATION WITH TERRASAR-X DATA

### A. TerraSAR-X data presentation

TerraSAR-X represents an interesting scenario for ship detection, since it can acquire high resolution polarimetric data from space [40]. The datasets exploited in this validation considers quad polarimetry from DLR's Dual Receive Antenna (*DRA*) campaign in 2010. Unfortunately, the quad polarimetric mode of TerraSAR-X is only experimental and this typology of data are not ordinarily acquired. Nevertheless, using quad polarimetric data, it is possible to compare the detection performance between quad and dual modes. The two datasets cover the off-shore area north of Gröningen (Holland) and the harbor area of Barcelona (Spain). The resolution of the data is  $1.18m$  in slant range and  $6.6m$  in azimuth, while the sampling is  $0.91m$  in range (equivalent to  $1.48m$  in ground range) and  $2.39m$  in



azimuth.

The North Sea data were acquired the 23<sup>th</sup> April and 12<sup>th</sup> April 2010 with an incidence angle of 28 degrees. The area is of particular interest for the algorithm validation, since in the middle of the acquisition area there is the *Alpha Venta* wind farm. This is composed of 13 wind turbines and one substation (umspannwerk) [41]. A schematic illustrating the location of the wind turbines is showed in Figure 9.a. The Barcelona dataset considered in this paper is composed of 2 acquisitions on the same days: 23<sup>rd</sup> April and 12<sup>th</sup> of April 2010. The central incidence angle for both the acquisitions is 33.8 degrees.

In this test, an initial multi-look of 3x5 (range x azimuth) is performed to make the pixel more squared on the ground. Subsequently the target moving window (before defined as  $w$ ) is 5x5. Considering the large over-sampling, the *ENL* is lower than the number of samples, ending up with about 38 independent looks (this is the reason why this value was used in the simulation). Considering the dimensions of the target of interest, this arrangement in window size was revealing the best. However, in case that the detection is focused on very small vessels, less pixels could be used. On the data available, using less pixels was still returning good detection capabilities however, the simulations performed in the previous section were suggesting possible problems with false alarms using small windows. For this reason, results with small windows are not presented here and in the future better ground truth will be employed to validate such window configuration. The big averaging window  $W_{tr}$  exploited to extract the value of  $\hat{t}_{sea}$  is 50 x 50 after the multi-look ending up with  $ENL \approx 10,000$  (the area covered is about  $\sim 600m \times 600m$ ). The parameters used for the detection are the same evaluated in the simulation section: i.e.  $T = 0.98$  and  $RedR = 2 * 10^{-3}$ , which returns a minimum target  $P_T^{min} \approx 0.22$ .

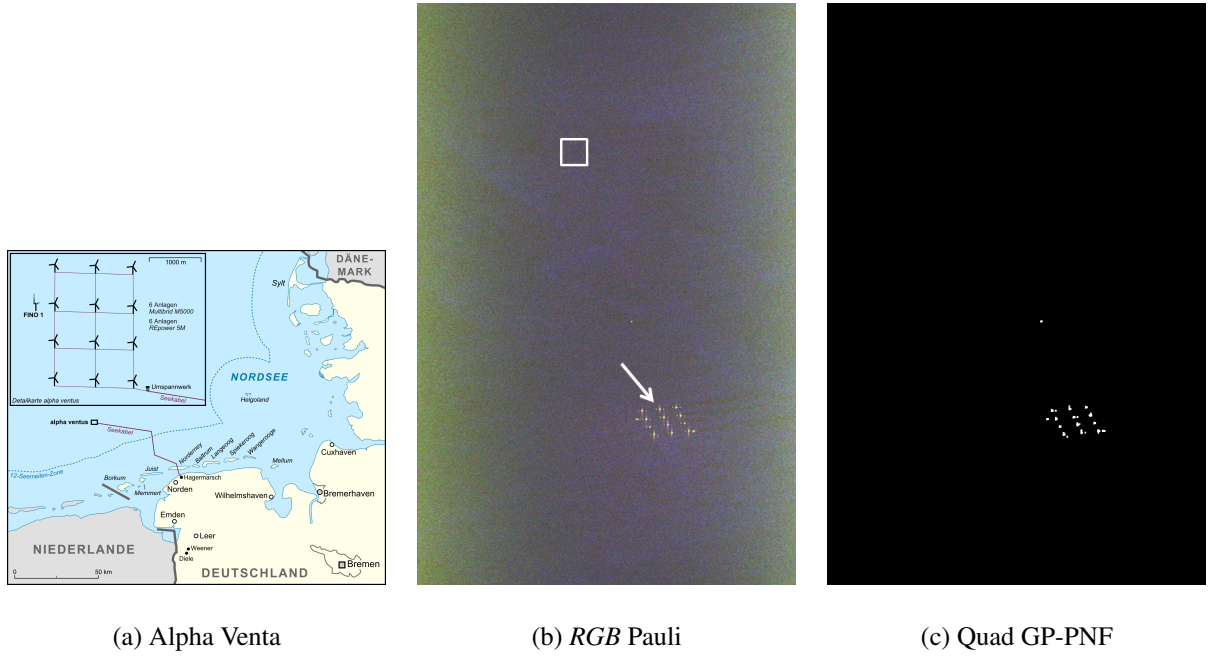


Fig. 9. TerraSAR-X Quad polarimetric data over Alpha Venta wind farm (North Sea, 23<sup>th</sup> April 2010): (a) Alpha Venta illustration (b) *RGB* Pauli composite image (c) GP-PNF detection with quad-pol.

## B. Validation results: North Sea

The Pauli *RGB* image of the area is illustrated in Figure 9.b.

The wind turbines are visible in the *RGB* image where the range direction is horizontal (left to right). The arrow indicates the turbine that was used to extract the signature for the previous simulations. No special rule was used to choose that specific turbine, since the signatures are relatively similar.

The polarimetric signature of the sea appears slowly to vary along the range direction due to incidence angle and noise effects for HV. For this reason, the dataset is valuable to evaluate the robustness of the proposed adaptive algorithm with respect to changes in the sea polarimetric signature  $\hat{t}_{sea}$ . Unfortunately, meteorological information at the time of the acquisition are not available, however, an easy way to have an idea about the difficulty of the detection exercise is to evaluate the maximum value of the sea backscattering in an averaging

481 window. In the present dataset the maximum value of the sea intensity in the VV polarization  
 482 is around 0.3, showing moderate wind conditions.

483 Figure 9.c depicts the GP-PNF mask exploiting quad polarimetric data. The mask is ob-  
 484 tained setting to 0 (i.e. black) all the pixels where  $\gamma_n < T$  and 1 where  $\gamma_n > T$ . Moreover,  
 485 merely for visualization purposes, every time that a point is detected it is expanded in the  
 486 mask to a squared area of 20x20 pixels. Again this is only to allow a good visualization of  
 487 the mask and an automatic algorithm will not need to perform this enlargement. This is also  
 488 useful to have a visual assessment of false alarms since even a single-pixel false alarm would  
 489 have a large visualized area in the mask.

490 The mask shows that the 13 wind turbines and substation (umspannwerk) are correctly  
 491 detected. Moreover, there is another target that is detected. Unfortunately, ground truths  
 492 are not available to confirm that it is a vessel, however its backscattering is particularly high  
 493 making us believe it is a genuine detection. An interesting point is that the adaptive selection  
 494 of the null is able to follow the changes of the sea surface even though  $\hat{t}_{sea}$  appears to change  
 495 from near to far range. In order to test the dual polarimetric version of the detector, Figure  
 496 10.a and Figure 10.b present the detection mask of the GP-PNF when the dual polarimetric  
 497 HH/VV and HH/HV modes are exploited.

498 Again all the turbines, the substation and the unknown-vessel are detected. This is because  
 499 these targets present a large backscattering in a wide portion of the target space, therefore  
 500 they will have a significant projection also in the subset observable by the dual-pol mode.

501 The detection over the second dataset in the North Sea are presented in Figure 11. The  
 502 maximum intensity of the sea in the VV polarization is around 0.25, showing a moderate sea  
 503 state.

504 As for the previous case, all the wind turbines and substation are detected with all the

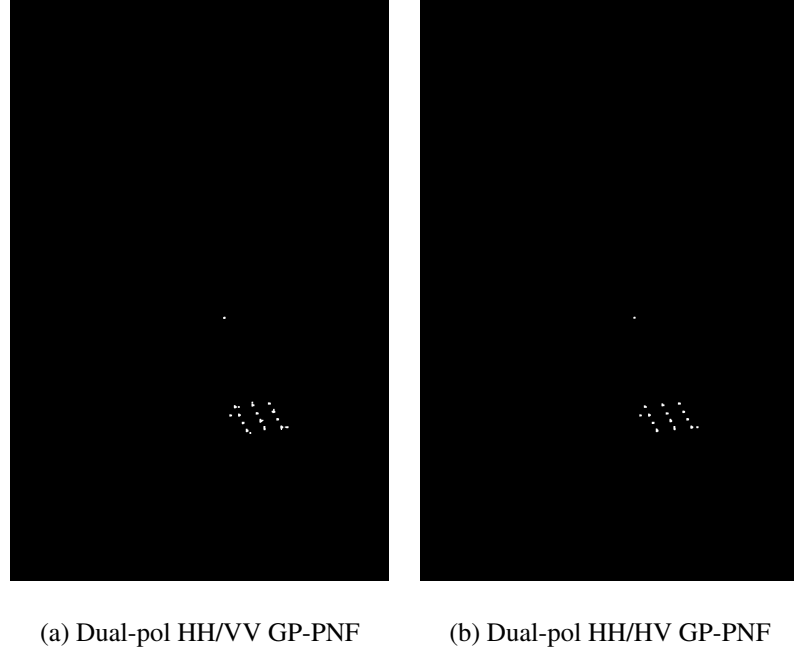


Fig. 10. TerraSAR-X detection over Alpha Venta wind farm (North Sea, 23<sup>th</sup> April 2010): (a) Detection with dual pol HH/VV GP-PNF (b) Detection with dual pol HH/HV GP-PNF.

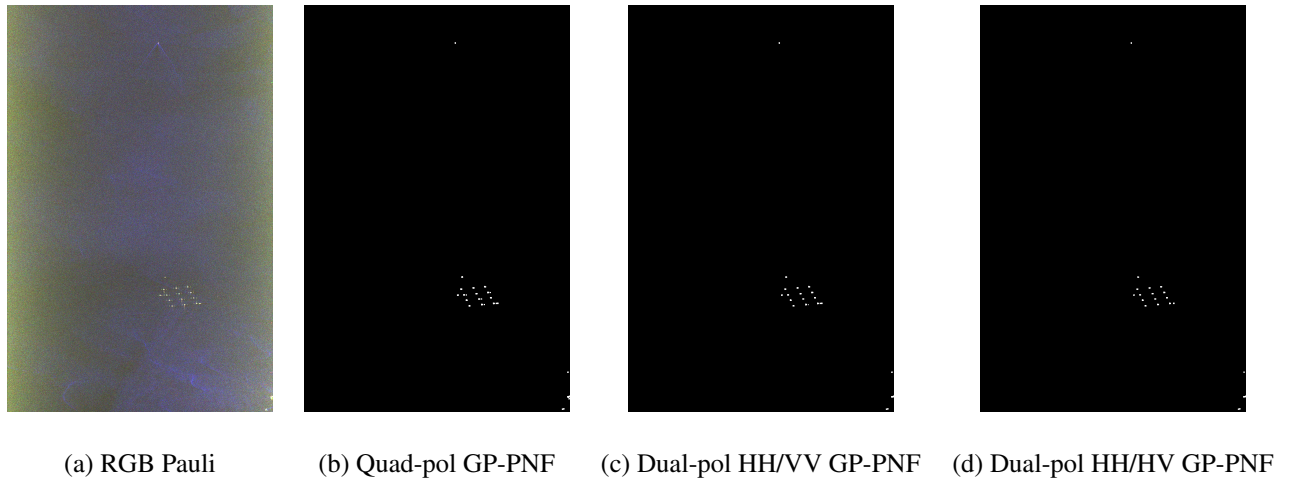


Fig. 11. TerraSAR-X detection over Alpha Venta wind farm (North Sea, 12<sup>th</sup> April 2010): (a) *RGB* Pauli composite image (b) Detection with GP-PNF quad-pol (c) Detection with GP-PNF dual-pol HH/VV (d) Detection with GP-PNF dual-pol HH/HV.

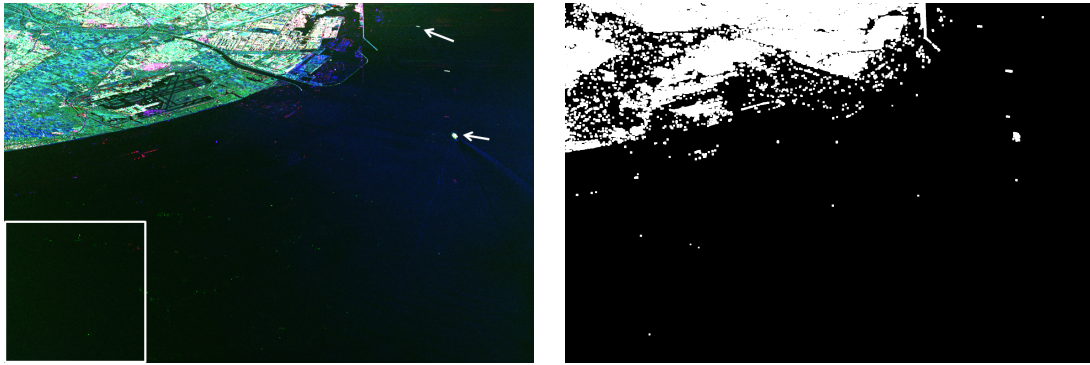
505 modes. Additionally, there are two bright areas in the images that are detected. The one  
 506 in the upper part of the image is clearly a vessel since its wake is visible. The other, just  
 507 north of the wind farm, is particularly bright and it is quite unlikely to be a false alarm (it is  
 508 probably a supervision boat). Unfortunately, ground truths are not available to confirm this  
 509 last theory.

510 Regarding the analysis of false positive, all the detection performed in these two exper-  
 511 iments do not present any false alarm (as long as the three very bright pixels are genuine  
 512 vessels).

### 513 *C. Validation results: Barcelona*

514 The second test considers the two Barcelona's datasets. Firstly, the 23<sup>rd</sup> of April is ana-  
 515 lyzed. Figure 12.a shows the *RGB* Pauli composite image. The sea return seems particularly  
 516 low, due to the low wind conditions. The most of the sea region is black in the *RGB*. In  
 517 the upper right corner, three bright points are visible. One of them is clearly a vessel due to  
 518 the wake. Moreover in the lower left part of the image, many green spots appear randomly  
 519 distributed. We believe that the most of those green points are due to image artefact partic-  
 520 ularly visible when the sea backscattering is low. However, in the same location where the  
 521 green spots appear there are several fish farms. Unfortunately, it was not possible to find any  
 522 credited photo or nautical chart of the area to confirm that they are not artefact.

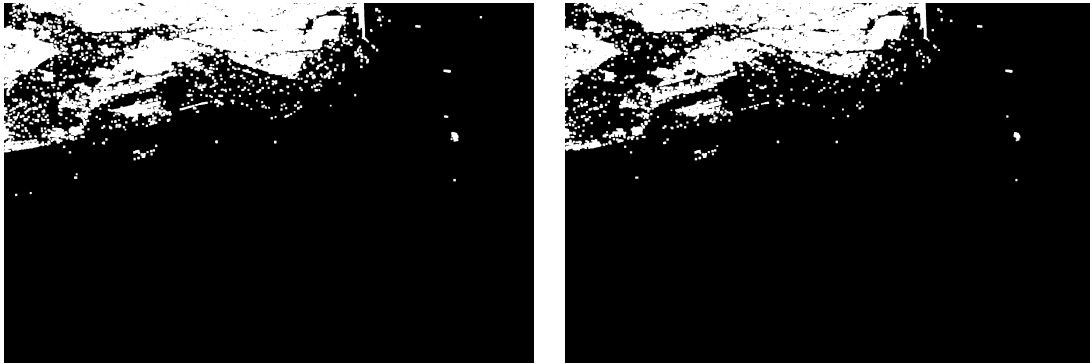
523 The arrows indicates two of the target signatures used previously in the simulation session.  
 524 Specifically,  $t_w$  is the vessel with the wake, while  $t_h$  is the upper vessel close to the harbor  
 525 entrance. The white rectangle indicates an area that in the following will be used to have  
 526 a zoom trying to spot small targets (i.e. using a smaller target window, as described in the  
 527 following).



(a) RGB Pauli

(b) GP-PNF quad-pol

Fig. 12. TerraSAR-X Quad pol date over Barcelona harbor (Mediterranean, 23<sup>rd</sup> of April 2010): (a) RGB Pauli composite image (b) Detection with GP-PNF quad-pol.



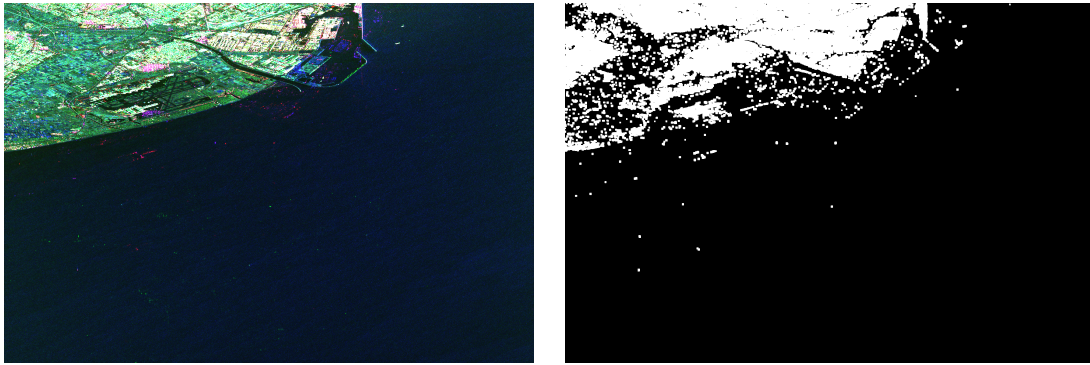
(a) Dual-pol HH/VV GP-PNF

(b) Dual-pol HH/HV GP-PNF

Fig. 13. TerraSAR-X quad-pol date over Barcelona harbor (Mediterranean, 23<sup>rd</sup> of April 2010): (a) Detection with GP-PNF dual-pol HH/VV (b) Detection with GP-PNF dual-pol HH/HV.

528 The detection masks with quad pol is presented in Figure 12, while Figure 13 shows the  
529 detection with dual-pol data.

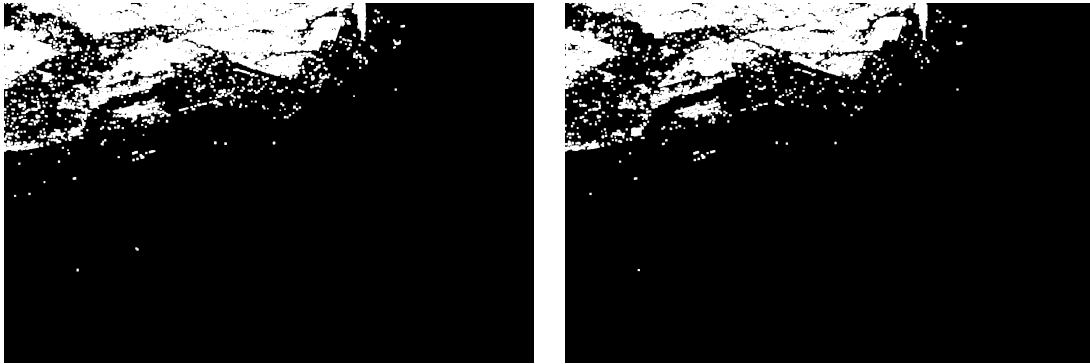
530 All the versions of the algorithms are able to detect the three ships. However, there are  
531 two bright red points (very likely ghost of two of the vessels) that cannot be detected with  
532 the HH/HV mode. This is because the scattering is mainly in HH-VV that is not completely  
533 observed by the HH/HV mode. Clearly, they are not genuine detection (and they can be  
534 corrected checking for the position of the nearby bright vessels), but in this experiment they  
535 are usefull to understand in which situation the HH/HV mode would fail. The green points



(a) RGB Pauli

(b) GP-PNF quad-pol

Fig. 14. TerraSAR-X Quad pol date over Barcelona harbor (Mediterranean, 12<sup>rd</sup> of April 2010): (a) RGB Pauli composite image (b) Detection with GP-PNF quad-pol.



(a) Dual-pol HH/VV GP-PNF

(b) Dual-pol HH/HV GP-PNF

Fig. 15. TerraSAR-X quad-pol date over Barcelona harbor (Mediterranean, 12<sup>rd</sup> of April 2010): (a) Detection with GP-PNF dual-pol HH/VV (b) Detection with GP-PNF dual-pol HH/HV.

in the *RGB* image are only partially detected (more details will be provided in the following section).

The second dataset was acquired the 12<sup>rd</sup> of April 2010. The images for the two dates are roughly co-registered over the land area with a simple correlation algorithm. Figure 14 shows the RGB Pauli with the GP-PNF quad-pol mask, while Figure 15 depicts the dual-pol GP-PNF detectors. Here, two vessels are visible close to the harbor and it is possible to detect them with all the modes.

In order to have an insight about the green spots in the left lower corner Figure 16 presents

544 a crop of the image with Pauli RGB and quad-pol GP-PNF masks for both the acquisitions.  
 545 Considering the targets are expected to be smaller the target window is modified from  $[5, 5]$   
 546 to  $[3, 3]$ . The latter correspond to an  $ENL \approx 8$ . The previous section was showing that when  
 547 the sea has a backscattering higher than 0.8,  $ENL = 8$  may introduce some false alarms.  
 548 Fortunately, this is not the case in this dataset, but care has to be put when other datasets are  
 549 considered. Finally, the detected points are not expanded as for the previous section, since  
 550 each of the detection should be more visible in this zoomed image.

551 Analyzing the two Pauli RGB images it can be observed that the most of the green spots  
 552 are located in exactly the same areas. The fact that the point did not move during the 11 days  
 553 is a hint that they represent either ambiguities from the nearby city or anchored targets (as  
 554 fish farms). In particular, the Y shaped red spot is an azimuth ambiguity. As a general idea,  
 555 if the GP-PNF is set to detect small targets it detects also the most of the ambiguities since  
 556 they represent heterogeneities over homogeneous background. A pre-processing algorithm  
 557 should be exploited in such cases. The detection masks, shows that in the two acquisitions  
 558 the same targets are detect (except for a point in the middle of the image that we presume  
 559 is a small vessel judging from the polarimetric signature in the RGB image). This is an  
 560 interesting result since it shows that the algorithm is able to detect the same targets in two  
 561 different sea conditions (i.e. it evaluates only the power coming from the targets).

562 The final experiment tests the dual-pol detectors over the weak targets. The detection  
 563 masks of the GP-PNF applied with HH/VV and HH/HV are presented in Figure 17. Com-  
 564 paring the results for dual- and quad-pol GP-PNF, the latter detects more points. Although,  
 565 all the detections correspond to bright points in the RGB image, ground truths of the area  
 566 are not available and it is not possible to know whether these points are genuine detections  
 567 or false alarms (please note, in this context ambiguities can be considered as true positives



568 even though they would be removed in an operative stage). Nevertheless, it is possible to  
569 see a general higher detection capability of the quad-pol GP-PNF. Moreover, it is hard to de-  
570 cide which dual-pol mode performs better, since both have a comparable number of detected  
571 points.

572 After this second analysis, some conclusions could be drawn regarding the importance of  
573 the cross polarization for detection of man made targets over sea clutter with TerraSAR-X.  
574 When the GP-PNF was focused on detection of medium/large vessels all the modes had sim-  
575 ilar performance, detecting all the turbines and points that can be visually interpreted as ves-  
576 sels in all the North Sea and Barcelona datasets. On the other hand, when the detection was  
577 focused on smaller vessels (and what was supposed to be fish farms), the quad-pol showed  
578 better performance compared to the dual-pol modes. Regarding, the best mode between  
579 HH/VV and HH/HV, it was not possible to draw conclusions with the available datasets due  
580 to the lack of accurate ground truth. However, considering the typology of scattering ex-  
581 pected by vessels and the fact that the sea can be very well characterized by using the two  
582 co-polarizations, the HH/VV mode should be advantageous compared to HH/HV. Further  
583 work will be carried out on this issue.

## 584 VI. CONCLUSION

585 In this paper an adaptive Geometrical Perturbation-Polarimetric Notch Filter (GP-PNF)  
586 for detection of maritime features (ship, buoys, icebergs, etc) was proposed. The GP-PNF  
587 detects the features which are polarimetrically different from a local homogeneous clutter  
588 background as it is the sea. The proposed algorithm is adaptive and it is able to select auto-  
589 matically the polarimetric signature of the sea (used to set the Notch) locally. The detector is  
590 initially developed for quad polarimetric data, since they assure the uniqueness of the target

characterization, however, a dual polarimetric version is proposed too, in order to take into account the situations when quad pol data can not be acquired.

The algorithm was tested on 4 quad polarimetric TerraSAR-X datasets acquired during the Dual Receiver Campaign in 2010 on areas including a wind farm (Alpha Venta) in the North Sea and the harbor of Barcelona. The detection masks are in agreement with available ground truth and expected targets in the area.

The comparison between dual and quad polarimetric GP-PNF showed very similar results when the GP-PNF was focused on medium/large vessels. However, when tested with small vessels (and fish farms) the quad-pol GP-PNF was able to detect more targets. But unfortunately accurate ground truth are not available to confirm that these are genuine detections. For the same reason was not possible to identify which mode between HH/VV and HH/HV performed better. However, considering the expected scattering from vessels and sea the HH/VV should be able to characterize better either sea and vessels. For this reason, HH/VV should be (at least theoretically) preferred to HH/HV.

The third part of the paper was dedicated to the test of the GP-PNF with Monte Carlo simulations. Specifically, two points were under analysis: the independence of the GP-PNF with respect to (i) the sea backscattering  $\sigma_{sea}$  and (ii) the specific sea polarimetric signature  $t_{sea}$ . The simulations showed notable performance with theoretical probability of detection  $P_D \approx 1$  and probability of false alarm  $P_F \approx 0$ . Moreover, further analysis were performed in order to understand in which circumstances the detector performance can reduce. Specifically,  $P_D$  is lower than 1 when the targets have a backscattering lower than a fixed minimum (which can be chosen) and  $P_F$  is higher than 0 when there are errors in the estimation of the sea signature (the value chosen for the Null).

As a future work, the probability density function (pdf) of the detector will be investigated

in order to perform an analytical assessment of the detector performance. Moreover, further validation with a large variety of sea states will be attempted, in order to understand the limits of the GP-PNF. With the same dataset, the best dual-pol mode between HH/VV and HH/HV will be investigated as well.

## VII. ACKNOWLEDGMENTS

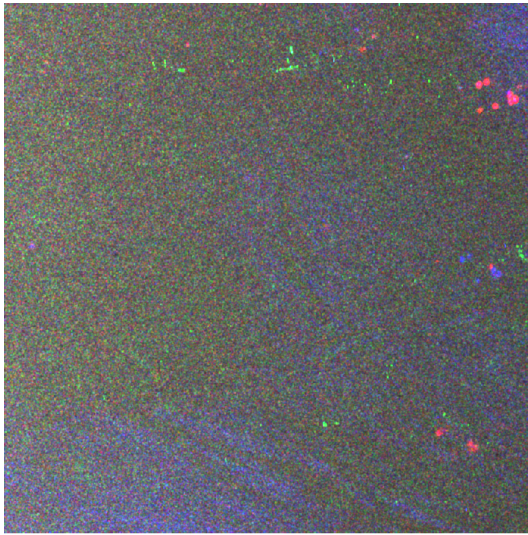
This work was partially supported by the ESA programme, "VAE actions to integrate new developments into EO services", ESRIN contract number 22568/09/I-EC. Also the author would like to thank eOsphere to have partially funded the work presented in this paper. TerraSAR-X data were provided by DLR in the framework of the AO for Dual Receive Antenna (DRA) 2010 campaign.

## REFERENCES

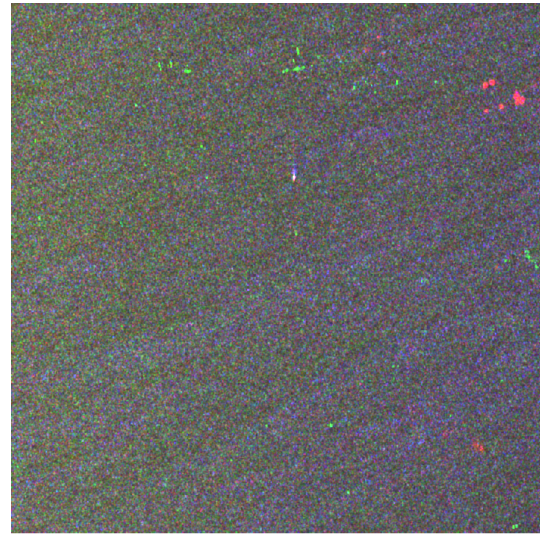
- [1] A. Marino, S. R. Cloude, and I. H. Woodhouse, "A polarimetric target detector using the Huynen Fork," *IEEE Trans. on Geos. & Rem. Sens.*, vol. 48, pp. 2357–2366, 2010.
- [2] A. Marino, S. R. Cloude, and I. H. Woodhouse, "Detecting depolarizing targets with satellite data: a new geometrical perturbation filter," *IEEE Int. Geos. & Rem. Sens. Symp. IGARSS*, 2010.
- [3] A. Marino and S. R. Cloude, "Detecting depolarizing targets using a new geometrical perturbation filter," *Proc. on EUSAR'10, Aachen, Germany, June*, 2010.
- [4] A. Marino, *A New Target Detector Based on Geometrical Perturbation Filters for Polarimetric Synthetic Aperture Radar (POL-SAR)*, Springer-Verlag, 2012.
- [5] V. Barele and M. Gade, *Remote Sensing of the European Seas*, Springer, 2008.
- [6] C. Liu, P. W. Vachon, and G. W. Geling, "Improved ship detection using polarimetric SAR data,," *IGARSS Geoscience and Remote Sensing Symposium*, vol. 3, pp. 1800–1803, 2004.
- [7] R. Touzi, "On the use of polarimetric SAR data for ship detection," *IGARSS Geoscience and Remote Sensing Symposium*, vol. 2, pp. 812–814, 1999.
- [8] R. Ringrose and N. Harris, "Ship Detection Using Polarimetric SAR Data," *SAR Workshop: CEOS Committee on Earth Observation Satellites*, 2000.

- 641 [9] D. J. Crisp, "The State-of-the-Art in ship detection in Synthetic Aperture Radar imagery," *Australiane Government*  
642 *Department of Defence*, 2004.
- 643 [10] D.J. Crisp and T. Keevers, "Comparison of ship detectors for polarimetric sar imagery," *OCEANS 2010 IEEE -*  
644 *Sydney*, pp. 1–8, 2010.
- 645 [11] F. Nunziata, A. Montuori, and M. Migliaccio, "Dual-polarized cosmo skymed sar data to observe metallic targets at  
646 sea," *IGARSS , Geoscience and Remote Sensing IEEE International Symposium*, pp. 2270–2273, 2011.
- 647 [12] A. J. Poelman, "Virtual polarization adaptation. a method of increasing the detection capability of a radar system  
648 through polarization vector processing," *Proceedings IEE*, vol. 128, No. 5., pp. 261–270, 1981.
- 649 [13] A. J. Poelman and K. J. Hilgers, "The effectiveness of multi-notch logic product polarization filters in radar for  
650 countering rain clutter," *Kluwer Academic Publishers*, 1992.
- 651 [14] K. Suwa, K. Yamamoto, C. Nonaka, A. Imamura, and T. Kirimoto, "A target detection algorithm using polarimetric  
652 notch filter," *Electronics and Communications in Japan (Part I: Communications)*, vol. 88, Issue 3, pp. 33–43, 2005.
- 653 [15] A. Marino, N. Walker, and I. H. Woodhouse, "Ship detection using SAR polarimetry. the development of a new  
654 algorithm designed to exploit new satellite SAR capabilities for maritime surveillance," *Proceedings on SEASAR,*  
655 *Frascati, Italy, January*, 2010.
- 656 [16] A. Marino, N. Walker, and I. H. Woodhouse, "Ship detection with SAR data using a notch filter based on perturbation  
657 analysis," *Proceedings on IGARSS, Honolulu, Hawaii, July*, 2010.
- 658 [17] A. Marino and N. Walker, "Ship detection with quad polarimetric terrasars-x data: an adaptive notch filter," *Proc. on*  
659 *IGARSS11*, 2011.
- 660 [18] J. S. Lee and E. Pottier, *Polarimetric radar imaging: from basics to applications*, CRC Press, Taylor & Francis  
661 Group, 2009.
- 662 [19] S. R. Cloude, *Polarisation: Applications in Remote Sensing*, Oxford University Press, 2009.
- 663 [20] S. R. Cloude and E. Pottier, "A review of target decomposition theorems in radar polarimetry.," *IEEE Transaction on*  
664 *Geoscience and Remote Sensing*, vol. 34, pp. 498–518, 1996.
- 665 [21] G. A. Deschamps and P. Edward, "Poincare sphere representation of partially polarized fields," *IEEE Transaction on*  
666 *Antennas and Propagation.*, vol. 21, pp. 474–478, 1973.
- 667 [22] G. Margarit, J.J. Mallorquí, J. Fortuny-Guasch, and C. López-Martínez, "Exploitation of ship scattering in polarimet-  
668 ric sar for an improved classification under high clutter conditions," *IEEE Transactions on Geoscience and Remote*  
669 *Sensing*, vol. 47, 2009.
- 670 [23] M. Brizi, P. Lombardo, and D. Pastina, "Exploiting the shadow information to increase the target detection perfor-  
671 mance in sar images.," *International Conference on Radar Systems, RADAR99*, 1999.
- 672 [24] K. Eldhuset, "An automatic ship and ship wake detection system for spaceborne sar images in coastal regions.," *IEEE*  
673 *Transactions on Geoscience and Remote Sensing*, vol. 34, pp. 1010 – 1019, 1996.

- 674 [25] K. Ouchi, S. Tamaki, H. Yaguchi, and M. Iehara, "Ship detection based on coherence images derived from cross  
675 correlation of multilook sar images," *IEEE Geoscience and Remote Sensing Letters*, vol. 1, 2004.
- 676 [26] A.J. Rye, F.G. Sawyer, and R. Sothinathan, "A workstation for the fast detection of ships," *Proceeding on IGARSS90*,  
677 vol. 3, 1990.
- 678 [27] M. Sciotti and P. Lombardo, "Ship detection in sar images: a segmentation-based approach.," *Proceedings of the*  
679 *2001 IEEE Radar Conference*, 2001.
- 680 [28] P. W Vachon, "Ship detection in synthetic aperture radar imagery.," *Proceedings OceanSAR, St. John s, NL, Canada*,  
681 2006.
- 682 [29] C.C. Wackerman, K.S. Friedman, W.G. Pichel, P. Clemente-Colon, and X. Li, "Automatic detection of ships in  
683 radarsat-1 sar imagery," *Canadian Journal of Remote Sensing*, vol. 27, 2001.
- 684 [30] M. Jeremy, G. Geling, M. Rey, B. Plache, and M. Henschel, "Results from the crusade ship detection trial: polari-  
685 metric sar.," *Proceeding on IGARSS 2002*, 2002.
- 686 [31] C. Brekke, S.N. Anfinssen, and Y. Larsen, "Subband extraction strategies in ship detection with the subaperture cross-  
687 correlation magnitude," *IEEE Geoscience and Remote Sensing Letters*, 2012.
- 688 [32] S. M. Kay, *Fundamentals of Statistical Signal Processing*, Prentice Hall, 1993.
- 689 [33] F. Nunziata, M. Migliaccio, and C.E. Brown, "Reflection symmetry for polarimetric observation of man-made metallic  
690 targets at sea," *IEEE Journal of Oceanic Engineering*, vol. 37, 3, pp. 384–394, 2012.
- 691 [34] R. Shirvany, M. Chabert, and J.-Y. Tourneret, "Ship and oil-spill detection using the degree of polarization in linear and  
692 hybrid/compact dual-pol sar," *IEEE Journal of Selected Topics in Applied Earth Observations and Remote Sensing*,  
693 2012.
- 694 [35] A. Marino and N. Walker, "Ship detection in variable sea states and depolarised sea clutter: a polarimetric notch  
695 filter," *Proceeding on POLinSAR*, 2011.
- 696 [36] A. Marino, S. R. Cloude, and I. H. Woodhouse, "Detecting depolarized targets using a new geometrical perturbation  
697 filter," *IEEE Transaction on Geoscience and Remote Sensing*, vol. In press, 2012.
- 698 [37] G. Strang, *Linear Algebra and its Applications*, Thomson Learning, 1988.
- 699 [38] C. Elachi and J. van Zyl, *Introduction To The Physics and Techniques of Remote Sensing*, John Wiley and Sons, 2006.
- 700 [39] F. T. Ulaby, Moore R. K., and Fung A. K., *Microwave Remote Sensing Volume 3*, The Artech House, 1986.
- 701 [40] S. Suchandt, H. Runge, and U. Steinbrecher, "Ship detection and measurement using the TerraSAR-X dual-receive  
702 antenna mode," *IEEE International Geoscience and Remote Sensing Symposium (IGARSS)*, pp. 2860 – 2863, 2010.
- 703 [41] "<http://www.alpha-ventus.de/index.php?id=80>," .



(a) RGB Pauli 23<sup>th</sup> April



(b) RGB Pauli 12<sup>th</sup> April



(c) Quad-pol GP-PNF 23<sup>th</sup> April



(d) Quad-pol GP-PNF 12<sup>th</sup> April

Fig. 16. TerraSAR-X quad-pol data over Barcelona harbor (Mediterranean): (a) Crop of RGB Pauli image of 23<sup>th</sup> April (b) Crop of RGB Pauli image of the 12<sup>th</sup> April (c) Detection with GP-PNF Quad-pol 23<sup>th</sup> April (d) Detection with GP-PNF Quad-pol 12<sup>th</sup> April.

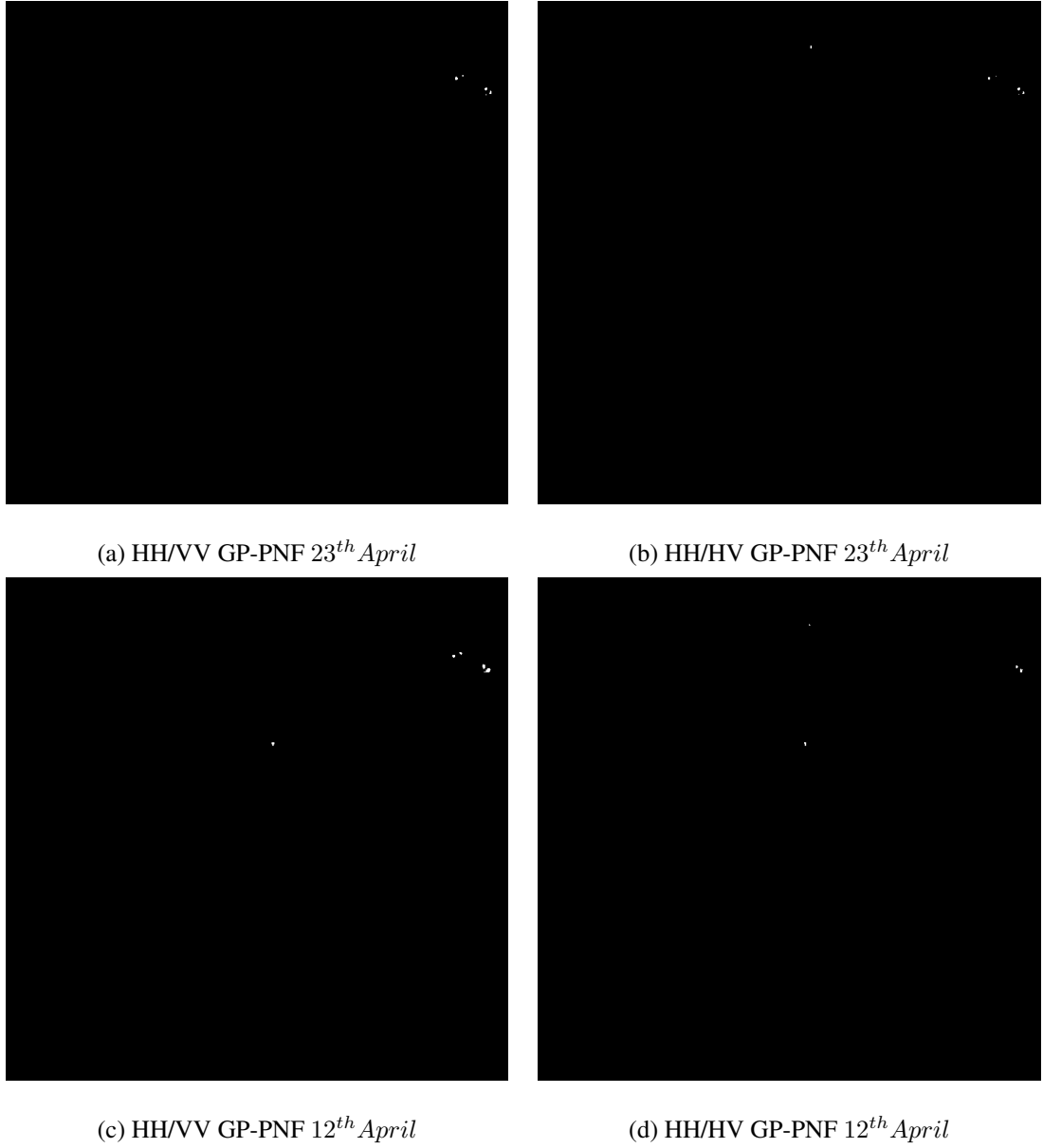


Fig. 17. TerraSAR-X over Barcelona harbor (Mediterranean): (a) Dual-pol HH/VV GP-PNF for 23<sup>th</sup> April (b) Dual-pol HH/HV for 23<sup>th</sup> April (c) Dual-pol HH/VV GP-PNF for 12<sup>th</sup> April (d) Dual-pol HH/HV GP-PNF for 12<sup>th</sup> April.